Journal of the European Ceramic Society 43 (2023) 6112–6121

Contents lists available at ScienceDirect

Journal of the European Ceramic Society

journal homepage: www.elsevier.com/locate/jeurceramsoc

Long-lasting ceramic composites for surface dielectric barrier discharge plasma actuators

K.O. Shvydyuk [a,*], F.F. Rodrigues [a], J. Nunes-Pereira [a,b], J.C. Páscoa [a], S. Lanceros-Mendez [b,c,d], A.P. Silva [a,*]

[a] C-MAST, Centre for Mechanical and Aerospace Science and Technologies, Universidade da Beira Interior, Rua Marquês d'Ávila e Bolama, 6201-001, Covilhã, Portugal
[b] CF-UM-UP, Centro de Física das Universidades do Minho e do Porto, Campus Gualtar, 4710-057 Braga, Portugal
[c] BCMaterials, Basque Center for Materials, Applications and Nanostructures, UPV/EHU Science Park, 48940 Leioa, Spain
[d] IKERBASQUE, Basque Foundation for Science, 48009 Bilbao, Spain

ARTICLE INFO

Keywords:
Ceramic composites
$MgO\text{-}Al_2O_3$
$MgO\text{-}CaZrO_3$
YSZ
DBD plasma actuators

ABSTRACT

The developed research presents a novel experimental study of the cost-effective $MgO\text{-}Al_2O_3$, $MgO\text{-}CaZrO_3$ perovskite, and thermally stable YSZ ceramic composites for DBD plasma actuators in aerospace applications. This study focuses on the implementation of ceramic DBD plasma actuators for aerodynamic flow control and ice creation mitigation. For this purpose, electrical power consumption analysis, induced flow velocities assessment, and mechanical and thermal characterization were performed. $MgO\text{-}Al_2O_3$ presented higher induced velocities than its zirconia-based counterparts of up to 3.3 m/s, and lower heat dissipation, achieving a ceiling temperature of 46 ºC, being thereby the best-suited candidate for active flow control mechanisms. In contrast, YSZ had very high-power consumption translated into a maximum surface temperature of 155.4 ºC, establishing itself for ice mitigation. This extensive research evinces that the strategic combination of the developed ceramics' thermo-mechanical, thermoelectric, and electromechanical properties allows them to be a promising breakthrough material for DBD plasma actuators.

1. Introduction

In the aeronautical and aerospace industries, ceramics are predominantly applied in thermal protection systems (TPS) and thermal barrier coatings (TBC). More specifically, advanced ceramics' ability to confer thermal insulation, lightness, high specific surface area, and thermal shock resistance make them suitable for shielding, instrumentation, and control purposes [1–6]. In this context, the present study addresses a novel approach for advanced ceramic composites as dielectric barrier discharge (DBD) mechanisms, considering their aforementioned favorable features [1–5,7].

The dielectric barrier discharge mechanism has been introduced for more than a century and a half by Ernst Werner von Siemens, originally for ozone production [8–10]. Nevertheless, in recent years, DBD's continuous research and technological development have attracted much attention for aeronautical and aerospace applications. Since the 1990s, surface dielectric barrier discharge actuators – which are devices supported in non-equilibrium plasma, capable of generating forces in the air without any moving parts – are considered a suitable technology, for aerodynamic active flow control and heat transfer phenomena, due to their easy implementation (i.e., simple construction), absence of moving parts, low mass, robustness, low power requirements, and fast response to electrical signals [11–13]. The ability to manipulate a flow field allows the improvement of the efficiency of several mechanical systems, by enhancing their performance through both fuel consumption and environmental impact reduction. Surface DBD plasma actuators have shown promising potential in modifying the laminar to turbulent transition, in delaying or reducing undesirable flow separation, in vortex shedding reduction, in lift enhancement and roll control, or as mechanisms to reduce drag [13]. In fact, the effectiveness of DBD mechanisms for boundary layer control considering different types of bodies, such as flat plates, cylinders, or airfoils has been the focus of multiple research [14–18]. Apart from aerodynamic applications, the thermal behavior of DBD plasma actuator devices may be exploited for active cooling of gas turbine blades through film cooling and heat generation for de-icing or anti-acing purposes. Liu et al. (2018) performed an experimental investigation focused on the comparison between the conventional electrical heating method and the DBD plasma-based method for ice

* Corresponding authors.
E-mail addresses: kateryna.shvydyuk@ubi.pt (K.O. Shvydyuk), abilio@ubi.pt (A.P. Silva).

https://doi.org/10.1016/j.jeurceramsoc.2023.05.040
Received 5 February 2023; Received in revised form 22 May 2023; Accepted 25 May 2023
Available online 26 May 2023
0955-2219/© 2023 The Author(s). Published by Elsevier Ltd. This is an open access article under the CC BY-NC-ND license (http://creativecommons.org/licenses/by-nc-nd/4.0/).

formation and accretion control [19]. More recently, Abdollahzadeh et al. (2022) performed an experimental parametric study to ascertain the influence of the main geometrical and physical features of the DBD plasma actuator on thermal and ice-sensing characteristics [20]. Moreover, considering the ice accretion phenomenon as a weather hazard impacting flight performance, and an ultimate threat to overall flight safety in cold climate conditions, Rodrigues et al. (2023) presented a review of the importance and potential of using DBD plasma actuators technology for ice mitigation. The review focuses on three main topics, i.e., thermal effects induced by DBD plasma actuators, plasma actuators' ability in deicing and ice formation prevention, as well as ice detection or sensing capability [21].

Broadly speaking, DBD plasma actuators' performance mainly depends on three major features: electrical parameters, geometry (i.e., configuration), and materials' properties of the dielectric layer. Furthermore, considering the dielectric layer, the trend research on novel materials, as well as materials modifications, continues to focus mainly on polymeric barriers based on their simplicity of use. Rodrigues et al. (2018) [22] presented a thermal characterization of DBD plasma actuators in which the dielectric barriers were made of Kapton, PLA, and PIB rubber. Bearing in mind that Kapton is the current dielectric trend in the DBD plasma actuators scientific community, the authors' study focused on different Kapton thicknesses, i.e., 0.3 mm, 0.6 mm, 0.84 mm, and 1.02 mm. Nunes-Pereira et al. (2022) [23] showed that Cirlex polyimide represents a suitable alternative candidate to Kapton polyimide for DBD plasma actuators, since Cirlex type dielectric barrier shows lesser electrical power consumption and dissipation, in addition to higher voltage operation limit, leading to higher induced velocities, higher mechanical power, and higher electromechanical efficiency. On the whole, Cirlex, when compared to Kapton, proved to be a more robust and durable dielectric barrier. Pons et al. (2008) [24] analyzed the surface degradation of two types of polymeric dielectric barriers, i.e., polymethyl methacrylate (PMMA) and polyvinyl chloride (PVC). A dielectric barrier of borosilicate glass was used as a control sample. Contrary to the PMMA and PVC polymers, which evidenced roughness, burning, and color changing, borosilicate glass showed to be more robust to both chemical and radiation exposure, since no obvious surface modification was detected.

Despite ongoing research on dielectric barrier materials for surface DBDs, in the literature, the studies have been mainly restricted to polymeric dielectric layers. Consequently, several authors highlight the necessity of different dielectric barriers that may improve the durability and effectiveness of these devices [22,25,26]. Specifically, polymers have been reported to be vulnerable to ion bombardment, radical species, and ultraviolet radiations that are emitted by plasma filaments in air at atmospheric pressure, thereby making them susceptible to material degradation, and, in turn, limiting the overall DBD mechanism lifetime due to dielectric barrier breakdown [11,24]. As a result, ceramics appear a suitable candidate for replacing polymers, since ceramics offer corrosion resistance, high- and low- temperature resistance, excellent dielectric properties, and heat conduction. Hehner et al. (2022) [25] conducted an experimental investigation of different materials and fabrication methods for dielectric barriers for surface DBD devices. The materials encompassed polyimide Kapton, PMMA, quartz glass, and ceramic Al_2O_3. The authors claimed that both glass and Al_2O_3 had more stable performance than the Kapton and PMMA over the entire range of tests conducted. Alumina was the more robust and durable dielectric barrier of the four materials assessed. Within this framework of thought, other research groups have used alumina in a coplanar DBD arrangement for industrial aims (i.e., plasma surface treatment, ozone generation, and adhesion improvement for film deposition) due to its high mechanical and dielectric strength, high resistivity, and small dielectric losses [27,28]. Studies focused on ABO_3 perovskite structures as a dielectric barrier have also been reported for carbon dioxide decomposition, at atmospheric pressure, due to their variety of dielectric properties [28,29].

Regardless of today's advancements in several technical and scientific fields, in standard aeronautical and aerospace applications of dielectric barrier discharge mechanisms, a significant effort for extensive research regarding the ceramic dielectric barrier is lacking. Only Bian et al. (2017) [30] focused on the material characterization and performance of two ceramic-based dielectric barriers, i.e., AlN and Al_2O_3.

This becomes particularly concerning since physical properties and plasma-chemical efforts are highly dependent on the material of the dielectric being used. In other words, both surface and electrical properties of the DBD plasma actuators are particularly influenced by the chemical composition of the dielectric barrier [27,28]. In an attempt to fill in the reported gap, this study focuses on the identification, study, and characterization of three ceramic compositions as dielectric barriers in surface DBD devices for active flow control, or de-icing aims. The present work introduces MgO-Al_2O_3 (MA), MgO-$CaZrO_3$ (MCZ), and Y_2O_3-doped ZrO_2 (YSZ) as dielectric barriers for DBD plasma actuators through electrical features, induced flow velocities, and thermal characteristics. The ceramic materials were selected based on the ceramic composites applied in aeronautical and aerospace engineering parts. Additionally, ceramic composites' mechanical and thermal properties were considered due to the vast implementation of ceramics on components subjected to extremely adverse hostile environments such as TPSs and TBCs applications.

2. Experimental procedure

2.1. Materials

Commercial (Acros Organics, Belgium) aluminum oxide (Al_2O_3, A) and (Alfa Aesar, USA) magnesium oxide (MgO, M) powders of high purity (wt%: 99 and 99, for A and M, respectively) were used as starting materials for the MgO-Al_2O_3 (MA) ceramics samples. Commercial (Alfa Aesar, USA) calcium zirconate ($CaZrO_3$, CZ) and magnesium oxide (MgO, M) powders of high purity (wt%: 99.2 and 99, for CZ and M, respectively) were used as starting materials to produce MgO-$CaZrO_3$ (MCZ) ceramic samples. For the three-phased yttria-stabilized zirconia (YSZ) ceramic system, commercial (Tosoh-Zirconia, Japan) 3 mol% yttria-stabilized zirconia (t-3YSZ), 8 mol% yttria-stabilized zirconia (c-8YSZ), in addition to (Acros Organics, Belgium) monoclinic zirconia (m-ZrO_2) powders of high purity (wt%: 99.8, 99.7 and 98.5 for t-3YSZ, c-8YSZ, and m-ZrO_2, respectively) were used as starting materials.

2.2. Sample manufacturing

The overall samples' manufacturing process was similar among all-ceramic composites. The starting raw powders were milled for 3 h at 500 rpm in a high-energy planetary mill (Fritsch, Pulverisette 6, Germany) in alumina – for the MA mixture – and zirconia – for the MCZ and YSZ mixtures – grinding bowls of 250 mL. Moreover, alumina and zirconia balls of 1 mm diameter (Fritsch), using isopropyl alcohol (Lab-Chem, USA) as a media, in a powder/alcohol/balls ratio of 1/1/2 were added. Afterward, all mixtures were dried at 50 °C for 24 h in air (Carbolite, NR200-F, United Kingdom) and, in due course, sieved (Retsch, AS200, Germany) in 63 μm so that the collected fine particles would be free of agglomerates and impurities.

Three different samples were considered, i.e., plates, bars, and disc specimens. The uniaxial pressing technique was adopted in a universal testing machine using rectangular (Instron 8800, 100 kN electromechanical actuator capacity, USA) and cylindrical (Shimadzu, AGS-X, 50 kN electromechanical actuator capacity, Japan) dies of high strength steel, previously lubricated, at 25 MPa for both rectangular specimens (60 mm × 60 mm), and disc specimens (diameter of 13 mm). The sintering process was carried out in air (Termolab, MLR, Portugal) following pre-sintering (for rectangular specimens cut into bars) and sintering steps (for all the remaining specimens). The pre-sintering

phase started with the rectangular specimens being heated at a rate of 5 °C/min up to 1200 °C with 120 min dwell. After the pre-sintering was completed, one of the rectangular plate specimens was cut into rectangular bars (5 mm × 5 mm × 50 mm), and the surfaces smoothened. Finally, the sintering stage, common to the rectangular plate, bar, and disc specimens took place: heating rate of 5 °C/min to the sintering temperature (1450 °C for the MCZ and YSZ, and 1600 °C for the MA ceramic composites) with 120 min dwell. In the finishing stage, grinding and polishing procedures were performed (Struers DAP-V, Denmark) with silicon carbide papers.

2.3. Sample analysis

2.3.1. Microstructure properties

Monitoring of the particle size distribution (PSD) was conducted throughout the fabrication stage to ensure that the ceramic systems would be manufactured as similarly as possible. The mixtures' particle size was evaluated using the laser diffraction method (Beckman Coulter, LS-200, USA).

X-ray diffraction (XRD) analysis was performed based on CuKα radiation on the bulk ceramic bar specimens using a diffractometer (Rigaku DMAX III/C, Japan). Data was collected between 5° and 90° (2θ). The results were analyzed by comparison with the theoretical ASTM XRD cards as follows: #71–1176 for magnesia (MgO), #46–1212 for aluminum oxide (Al_2O_3), #35–0790 for calcium zirconate ($CaZrO_3$), #50–1089 for t-3YSZ, #49–1642 for c-8YSZ, #37–1484 for m-ZrO_2, and #77–1193 for magnesium aluminum oxide ($MgAlO_4$).

Scanning electron microscopy (SEM) (Hitachi S-2700, Japan) was performed for microstructure imaging by applying an accelerating voltage of 20 kV. Thermal etching was conducted at 1305 °C (for YSZ and MCZ samples) and 1440 °C (MA sample), for 30 min with 10 °C/min heating and cooling rates. Afterward, the specimens were coated with an ultra-thin gold layer using a turbomolecular pump coater (Emitech K550 Gold Sputter Coater, Quorum Technologies, UK).

Apparent porosity, as well as apparent and relative bulk densities, were determined according to the ASTM C-20 standard [31]. For each ceramic composition, results are presented as an average of seven measurements and the error associated with the standard deviations. Theoretical densities values of the previous XRD cards were used to compute the relative densities of the manufactured samples by applying the rule of mixtures, Eq. 1.

$$\rho_{th} = \sum_{i=1}^{n} v_i \times \rho_i \quad (1)$$

where v_i indicates the volume fraction of the element i, ρ the theoretical density of the element i, and n the number of ingredients of the mixture.

2.3.2. Mechanical properties

The dynamic Young's modulus was experimentally obtained based on the impulse excitation technique (IET) applied on bar specimens of approximately 5.0 × 4.5 × 45 (mm), according to the non-destructive standard test method ASTM C1198 – 20 [32] (GrindoSonic MK7, Belgium). A Poisson ratio of 0.25 was considered.

The determination of flexural strength was performed according to the ASTM C1161 – 18 [33], applying the three-point test (Shimadzu AGS-X, Japan) on the same bar specimens, with a crosshead speed of 0.5 mm/min, and an outer support span of 40 mm. After that, similar broken parts from flexural tests of each composition were embedded in an epoxy resin (EpoxiCure 2 Epoxy Resin, Buehler, USA) and the surfaces were diamond polished down to 1 μm. The samples were tested for hardness and fracture toughness via the indentation technique as described in the ASTM C1327–15 standard [34]. Measurements of the latter parameters were performed in the Vickers hardness testing machine (Mitutoyo AVK – C2, Japan) applying 100 N for 15 s. Cracks emerging from the vertices of the indentations were used to calculate the fracture toughness.

2.3.3. Thermal properties

Thermal conductivity was computed through thermal diffusivity and specific heat experimental determination according to the laser flash analysis (LFA) standard test method ASTM E1461 – 13 [35]. For the evaluation of the thermal conductivity, the disc specimens (diameter of 12.55 ± 0.5 mm), were tested on a laser flash apparatus (LFA 457 MicroFlash, Netzsch, Germany) after applying a high emissivity coating (Kontakt-Chemie 76009-AG, Graphit 33 Spray, Belgium) on the ceramic specimens' surface to improve their ability to absorb the applied energy. The thermal conductivity of the ceramic samples was tested in a temperature interval ranging from room temperature of 30 °C up to 900 °C in a controlled inert atmosphere. In addition, a reference material (Pyroceramic, Order number 6.256.1–94.0.03, Netzsch, Germany), was tested simultaneously with the ceramic samples to compute the specific heat of the ceramic specimens and for calibration.

The coefficient of thermal expansion was determined through thermomechanical analysis (TMA). The TMA test was performed according to the ASTM E831 – 06 [36] standard test method by using a thermomechanical analyzer device (TMA 402 F1/F3 Hyperion, Germany) to determine the linear thermal expansion of the ceramics specimens when subject to a constant heating rate of 5 K/min. The coefficient of thermal expansion was evaluated upon a temperature interval ranging from − 110 °C to 980 °C in a controlled inert atmosphere. The mean coefficient of linear thermal expansion was determined with a pretest applied load in the interval of 0.2 N. A reference material (Fused Silica, Serial number 35859, Netzsch, Germany), was also used for accuracy assessment and calibration purposes.

2.3.4. DBD characterization

Electrical tests were performed to evaluate the feasibility of the different ceramic materials as dielectric barriers for DBD plasma actuators using several equipment (Fig. S1). The DBD plasma actuators were supplied by an AC high-voltage and frequency power source (PVM 500, Information Unlimited, USA) that allows voltage amplitudes up to 20 kV peak to peak (kVpp), and frequencies between 20 and 50 kHz. To monitor and record the voltage and current waveforms, a digital oscilloscope (PicoScope 5443 A, Pico Technology, UK) was used and connected to a high-voltage probe "Secondary Ignition Pickup" (MI074 Secondary Ignition Pickup, UK).

The dielectric barrier discharge plasma actuators were assembled and tested using the three different ceramic rectangular plate specimens as a dielectric barrier. The electrodes (40 mm in length and a thickness of 80 μm) of DBD plasma actuators were made of copper tape and asymmetrically mounted on either side of the dielectric barrier with a 1 mm gap between them [10,37,38]. Additionally, the electrodes were mounted with a misalignment of 10 mm (in the spanwise direction), as shown in Fig. S2a, allowing to generate a plasma discharge with a spanwise length of 30 mm. The width of the exposed electrode was 10 mm, whereas the enclosed one was 20 mm to certify that the plasma discharge extension would not be limited. Moreover, Fig. S2a represents the ceramic dielectric barrier glued with copper tape electrodes and Kapton tape as protection material to shield the covered electrode. The electrical experimental tests were conducted under environmental conditions of approximately 22 °C and 40 – 50% relative humidity.

The Electrical Current Method and the Electric Charge Method, well documented and explained by Ashpis et al. (2012) [39], were applied. The waveforms were collected with a sampling rate of 125 MS/s and a vertical resolution of 14 bits, which resulted in an uncertainty of approximately 1%. For the Electrical Current Method, a metal film resistor (Robert Mauser, Lda., Portugal), with an impedance of 100 Ω and 1% of tolerance was used, while for the Electrical Charge Method, the resistor was replaced by a ceramic disc capacitor E222M (Robert Mauser, Lda., Portugal), with a characteristic capacitance of 10 nF and a tolerance of 10%. The Electrical Charge Method allowed to obtain the Lissajous curves and corroborate the results of the Electrical Current Method [39,40].

After the power consumption was determined, the fluid dynamic characterization was performed to study the mechanical performance of each plasma actuator. The velocity of the plasma-induced flow was assessed by using the stainless-steel Pitot tube (167–6 model, Dwyer, USA). The experiments were conducted for distances of 10 mm and 15 mm between the exposed electrode and Pitot tube, as shown in Fig. S2b. In addition, the velocity was acquired during a time interval of 10 s, at a sampling rate of 1 sample per second, by using a micromanometer (Extech HD 350, UK) with a resolution of 0.01 m/s and an accuracy of 1% full-scale.

Finally, the temperature effect on the plasma discharge was analyzed using a thermal imaging camera (FLIR E50, Teledyne FLIR, USA) with a resolution of 240 × 180 pixels and 2% of uncertainty. The measurements were performed on the upper side of the dielectric plasma actuators from 130 mm and 210 mm height for the zirconia and alumina-based ceramics, due to their sizes, respectively. The infrared images were captured immediately after the stoppage of plasma discharge, which lasted for a total operation interval of 300 s, to ensure temperature stabilization. For the temperature analysis, the plasma actuators were painted with black matte ink with an emissivity of 0.97 [41] as shown in Fig. S3.

3. Results and discussion

3.1. Particle size distribution and microstructure

The particle size distribution of the MA, MCZ, and YSZ ceramic composite mixtures evidenced heterogeneous data [42]. After milling, the MA mixture presented a $d_{50} = 0.6$ μm and a $d_{90} = 1.8$ μm. Followingly, MCZ showed a $d_{50} = 0.8$ μm and a $d_{90} = 2.5$ μm. Lastly, the YSZ powder mixture had the highest particle size for the $d_{50} = 0.9$, however lower $d_{90} = 1.6$ μm (Table S1).

Representative SEM micrographs of the sintered ceramic composites – MA, MCZ, and YSZ – are presented in Fig. 1a, 1b, and 1c, respectively. Fig. 1a shows that alumina micrographs are characterized by the presence of a multiformity of grains both in size and geometry. Moreover, in the MA ceramic composite microstructures, an irregular shape of the grains and high porosity is observed, which is illustrative of incomplete sintering [27,43]. Grains are observed in two typical sizes: most are small with a rounded and faceted shape, with a size up to 0.5 μm, and others larger with an elongated shape, with a width of up to 1 μm and length up to 1.8 μm. Figs. 1b and 1c depict the micrographs for the zirconia-based composites. By comparing the two, it is evident that the milling process of YSZ fomented a notably homogeneous grain size distribution, which contributed to higher densification. Contrastingly, MCZ microstructure features differences with calcium zirconate (bigger and light gray) and magnesium oxide grains (smaller and dark rough texture). The average size of MgO grains is 1.2 μm and, in turn, $CaZrO_3$ grains which are rounded with a faceted shape have a size of up to 3 μm. YSZ grains are shown as round, the majority of them smaller than 0.3 μm, with some larger grains with diameters up to 0.8 μm.

The following Fig. 2 presents the XRD analysis of the MA, MCZ, and YSZ ceramic composites.

For MA several intensity peaks were identified, the majority of them corresponding mainly to Al_2O_3 (Al, with 2θ of 35°, 44° and 58°) or $MgAl_2O_4$ (MAl, 2θ equal at 45° and 65°). In the MCZ sample, the majority of the diffraction peaks coincide with the peaks of $CaZrO_3$ (CZ, namely 2θ equal at 32°, 45°, 56°, and 58°), whereas only some are of MgO (M). The XRD analysis for the YSZ specimens reveals that all three phases, i.e., c-8YSZ and t-3YSZ, (2θ of 30° and 50°) and m-ZrO_2 (2θ of 28° and 32°) are present in the ceramic composite.

In terms of relative porosity analysis (Table S2), MA ceramics show a high porosity, approximately 7.0%. Contrastingly, zirconia-based ceramics, MCZ and YSZ, exhibit porosity values inferior to 0.5%. Additionally, MA porosity data also exhibit a higher dispersion in experimentally measured results, i.e., 0.93%.

Regarding the density data, for MA, the incomplete sintering process resulted in a relative density of 71.1%, when compared to MCZ and YSZ

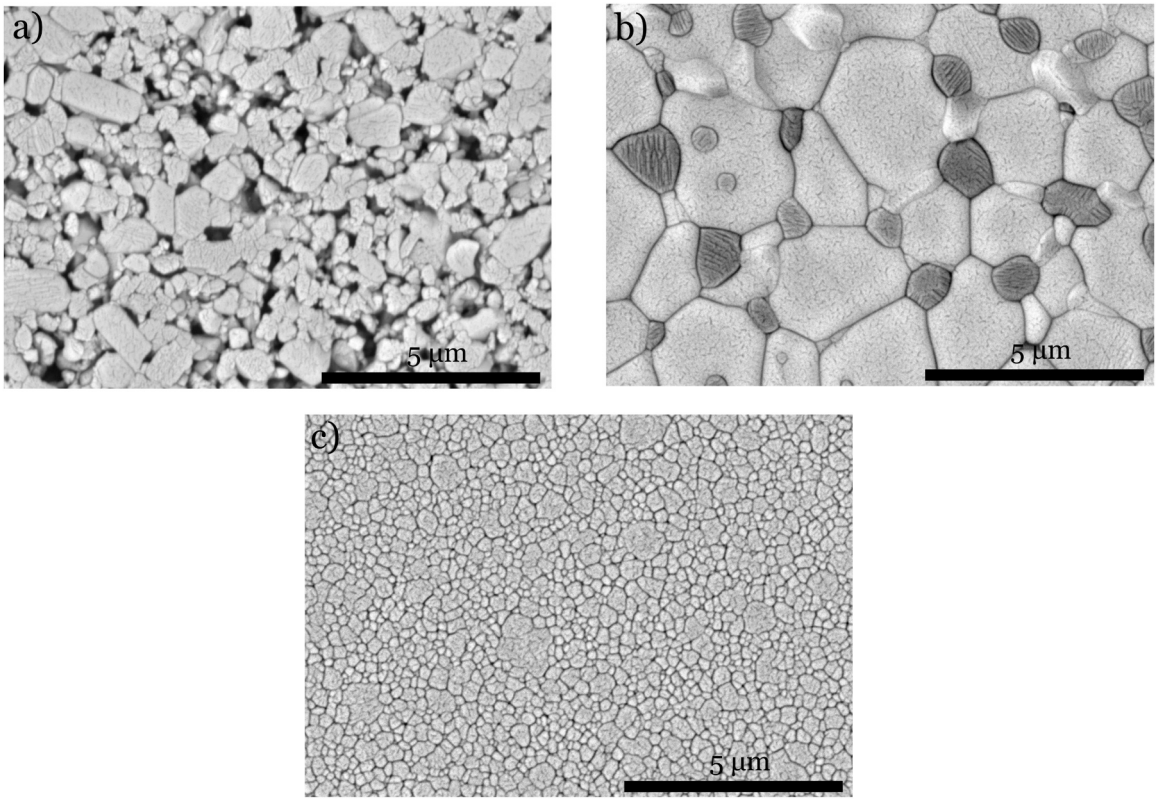

Fig. 1. Microstructural features for sintered composites. SEM micrographs of polished surfaces (a) MA, (b) MCZ, and (c) YSZ.

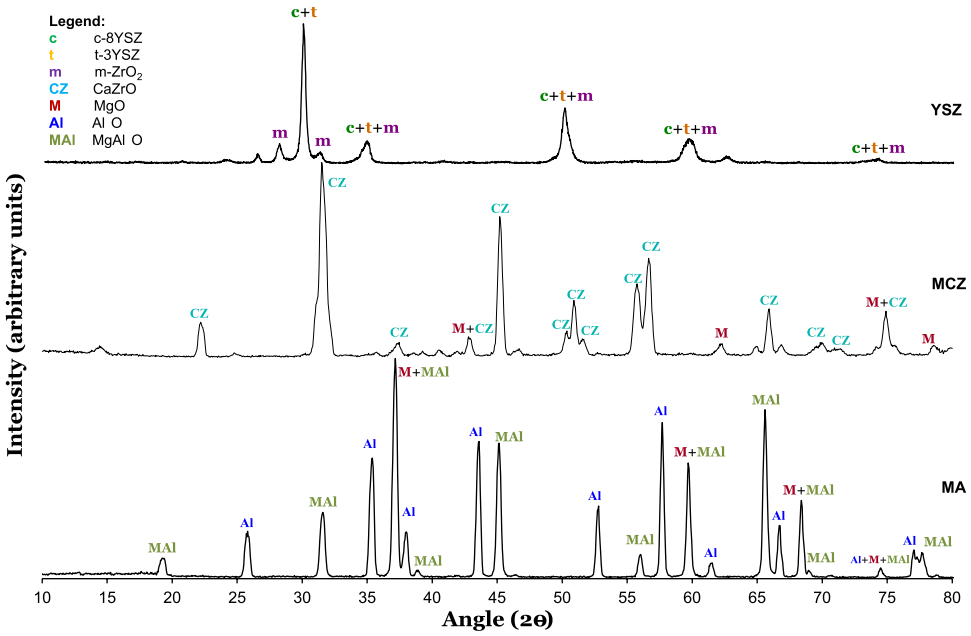

Fig. 2. XRD patterns of the MA, MCZ, and YSZ ceramic composites.

ceramics, which showed relative densities of 99.95% and 97.95%, respectively. In addition, the error associated with the measurements is under 1%.

3.2. Mechanical and thermal analysis

The mechanical characterization of the manufactured advanced ceramics composites, i.e., MA, MCZ, and YSZ was also analyzed. Table 1 presents the results of the conducted tests for both mechanical and thermal analysis.

The MA samples with a porosity of 7% may show some mismatch when compared to dense alumina ceramics values of Young's modulus of 340 – 380 GPa [44,45], flexural strength of 280 – 420 MPa [1,46,47], and hardness of 15 – 22 GPa [47,48]. This is strongly related to the so-called porosity dependence of materials properties [49,50]. In terms of fracture toughness, the MA composite obtained value is consistent with the values mentioned in the literature of 3.5 – 5.5 MPa.mm$^{1/2}$ [44].

Contrastingly, owing to the extremely low porosity content, and therefore obtained dense MCZ and YSZ ceramics specimens, the values of their mechanical features were in accordance with the literature. For the MCZ, the typical figures of Young's modulus, 228 GPa [51], flexural strength 250 – 270 MPa [52,53], hardness, 7.5 – 7.8 GPa [54,55], and fracture toughness, 2.5 – 2.6 MPa.mm$^{1/2}$ [54,55], are reported. For the YSZ, the guidelines' figures of Young's modulus, 210 – 220 GPa [56], flexural strength, 786 MPa [57], hardness, 12.5 GPa [58], and fracture toughness, 4.1 – 6.0 MPa.mm$^{1/2}$ [58,59], are obtained.

For the thermal properties, Table 1 shows that MCZ has a higher thermal conductivity than MA, which in turn has a higher thermal conductivity than YSZ – regardless of the temperature interval considered. Nevertheless, the thermal conductivity recorded for the MA sample is remarkably low. Sun J. et al. (2014) [60] explain that, by increasing porosity, ceramic's solid-phase heat conduction decreases, regardless of the temperature range studied, whilst the gas-phase heat conduction and thermal radiation rise. Thus, the overall thermal conductivity diminishes [60,61]. In contrast, for the MCZ [55] and YSZ [62] ceramics, the thermal conductivity values are in line with the literature.

Moreover, the values for CTE show that independently of the ceramic chemical compositions, increasing temperature leads to an increase in the thermal expansion coefficient. Bearing in mind the values indicated in the literature, it was concluded that MA [44], MCZ [63–65], and YSZ [66,67] CTE values are coherent with the reported in the literature. The CTE measurements associated error was inferior to 10^{-6}.

Table 1
Experimentally obtained mechanical properties (Young's modulus, flexural strength, hardness, and fracture toughness) and thermal properties (thermal conductivity and thermal expansion coefficient – the latter with an associate error inferior to 10^{-6}).

Mechanical Properties		**MA**	**MCZ**	**YSZ**
Young's Modulus [GPa]		317 ± 2.2	213 ± 0.2	197 ± 0.2
Flexural Strength [MPa]		103 ± 8.8	318 ± 16.5	740 ± 31.4
Hardness [GPa]		4.8 ± 0.1	7.3 ± 0.5	13.1 ± 0.6
Fracture Toughness [MPa.mm$^{1/2}$]		3.6 ± 0.1	2.7 ± 0.5	5.1 ± 0.6
Thermal Analysis				
Thermal Conductivity [W/(mK)]	30 – 100 °C	3.9 ± 0.2	5.3 ± 0.3	2.7 ± 0.1
	30 – 300 °C	3.3 ± 0.4	4.4 ± 0.7	2.5 ± 0.2
	30 – 600 °C	2.8 ± 0.6	3.7 ± 0.9	2.3 ± 0.2
Thermal Expansion Coefficient [10^{-6}/°C]	30 – 100 °C	5.8	8.4	9.3
	30 – 300 °C	6.4	8.7	9.7
	30 – 600 °C	7.1	9.3	10.1

3.3. DBD characterization

The Electric Current Method and the Electric Charge Method were explored to evaluate the electrical behavior of the different DBD devices. In this sense, the viability of the three ceramic composites, as dielectric barriers for DBD plasma actuators, was validated. The average power consumed by the three ceramic composites DBD plasma actuators is shown in Fig. 3 as a function of the applied voltages at a frequency of 24 kHz. The average electrical consumption was evaluated by using the Current Method, while the Charge Method allowed for corroborating the results. The average electric power consumption results showed an error

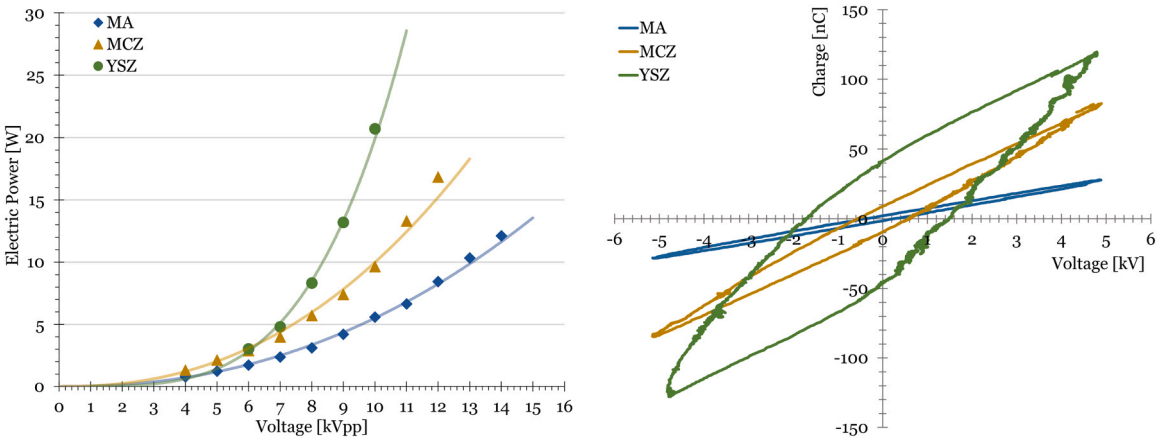

Fig. 3. MA, MCZ, and YSZ ceramic composites electric power consumption (a) and dielectric Lissajous curves (b) comparison at 10 kVpp.

lower than 2% based on the resistor's tolerance of 1% and the high resolution of the digital oscilloscope. Whenever the error bar is not visible, it means that it is contained by the different ceramics' markers (green, yellow, and blue) due to the high precision of the equipment used – explained throughout 2.3.4. section. On the other hand, the charge values showed an error lower than 5%, due to the slightly higher uncertainty of the capacitor in comparison to the resistor.

The power consumption parameter in the all-embracing DBD plasma actuator analysis is of utmost importance, in particular, for the comparative analysis of different actuator designs. Moreover, in terms of the practical implementation of flow control systems for aeronautical and aerospace applications, power consumption is required for a cost-benefit analysis of the system [10].

Fig. 3a shows that the average power consumed by the three ceramic dielectrics increases with the increasing input voltage. Until, approximately, 6 kVpp, i.e., for the low-voltage range, the power consumption shows similar behavior for MA, MCZ, and YSZ ceramic samples. Afterward, however, different tendencies – depicted by the fitting curves – arise for each dielectric. It must be emphasized that although the behavior for the low-voltage range mentioned is claimed to be similar, the magnitude of the values measured of the average power consumed by the ceramic composites is quite heterogeneous, this is, at 6 kVpp the corresponding power consumptions are, approximately, 3.0 W for YSZ, 2.9 W for MCZ, and 1.7 W for MA.

Moreover, at higher voltage levels, i.e., from 7 kVpp on, it is noticeable that the power consumed by each DBD plasma actuator device depends strongly on the material. More precisely, the YSZ curve depicts the sharpest increase of power consumption of all materials for the different input voltages, whereas MCZ shows a slightly slower (than YSZ) but still somehow rapid rise. Subsequently, MA ceramic represents a more regular growth in power consumed for the voltage interval applied. Besides the stated, it is also possible to infer that the YSZ ceramic has the lowest operating limit of 10 kVpp, followed by MCZ with a maximum input limit of 12 kVpp, and, finally, MA shows the highest operating limit of 14 kVpp. The operating limits were evaluated by considering the transition of the plasma discharge to an unstable and markedly filamentary regime, since, at this stage, for the wide range of input voltages analyzed, none of the specimens fractured or deteriorate to a level that they could no longer be tested. Therefore, the higher the input voltage the ceramic material is capable of supporting without causing marked, or, profound degradation, the broadest thus the operating range of the actuator [23,25,68].

To complete the electrical analysis, the Electric Charge Method allowed to compute the Lissajous curves, shown in Fig. 3b, for the three ceramic composites DBDs, for 10 kVpp input voltage. Dielectric Lissajous curves for MA, MCZ, and YSZ composites at different voltages are shown in Fig. S4. If the input voltage is in a low-level range, the imposed electrical field is weak and therefore incapable of generating plasma. In this case, the Lissajous figure consists of a straight line once the charge varies proportionally to the voltage and the system assumes a purely capacitive behavior [69]. Contrastingly, if the input voltage is in a considerable high-level range, and, thus, is capable of inducing a high electrical field, the Lissajous plot opens (spreads) in a geometry of a convex figure. Lissajous figures, also known as voltage-charge cyclograms, allow inferring the power consumed per cycle by computing the area inside a particular closed curve for that specific cycle period. For the surface DBD plasma actuators, the discharge process is not characterized by a constant geometrical plasma shape, it is more complex since it is time-varying in terms of discharge properties and behavior. The geometric shape of the overall discharge may change throughout the discharge active phase, owing to the accumulation of charges on the dielectric material surface, which will dictate the electric fields of the following discharges of the voltage AC sinusoid supply. Accordingly, changes in the shape of the discharge region occur and have a direct influence on the discharge capacitance, leading to so-called almond shaped Lissajous curves [70].

In Fig. 3b, the Lissajous curve for MA ceramic composite depicts a very closed shape and an especially sharp transition from the capacitance regime (in which no plasma discharge occurs) to the discharge regime (in which plasma discharge occurs). Despite the characteristic geometry of the cyclogram, the represented behavior agrees with the data on power consumption. In other words, MA ceramic presented the lowest power consumption values and, therefore, it also shows a very closed (i.e., narrow) Lissajous curve which is translated into low power consumption.

The Lissajous curves for MCZ ceramic, similar to the MA, represent a somewhat narrow shape and a distinctly sharp transition from the capacitance regime to the discharge regime. On the other hand, the Lissajous curve for the YSZ ceramic composite depicts a more commonly recognized [71] shape and behavior among the three dielectrics. YSZ's cyclograms have a convex geometry – that was not observed for the MA ceramic, nor for the MCZ – presenting well-defined slopes to easily assess the cold and effective capacitances of the assembled DBD plasma actuator device.

Moreover, Fig. 3b shows that the total charge transferred (assessed through y–axis) to the ceramic composites is, approximately 25 nC for MA, 80 nC for MCZ, and 120 nC for YSZ. The breakdown voltage (analyzed through x–axis), which determines the onset ignition of the plasma discharge, is highest for the YSZ (≈ 1.5 kV), followed by MCZ (≈ 0.6 kV), and finally, by MA (≈ 0.2 kV).

To evaluate the efficiency of the different DBD plasma actuators, for active flow control applications in aeronautical and aerospace fields, the induced flow velocities were measured by the Pitot tube technique (Fig. S2b). The induced velocities obtained experimentally were tested

for horizontal (x–direction) distances, between the exposed electrode and the Pitot tube, of 10 mm (Fig. 4a) and 15 mm (Fig. 4b), at the nearest point to the wall (y = 1.5 mm). Whenever the error bar is not visible, it means that it is contained by the different ceramics' markers (green, yellow, and blue) due to the high precision of the equipment used – explained throughout 2.3.4. section.

According to Fig. 4a, MA was the ceramic system capable of inducing higher velocities, approximately 3.0 m/s in comparison to the maximum achieved velocities of, about, 2.4 m/s and 2.2 m/s for MCZ and YSZ, respectively.

Nevertheless, it is noted that alumina-based ceramic required higher input voltages to generate flow velocities, i.e., the micromanometer was only able to register data starting from input voltages in the range of 11 kVpp for the MA, contrastingly with the 8 kVpp for MCZ and YSZ. Worth noting that once the difference between the induced velocities for 7 kVpp and 8 kVpp of MCZ is practically negligible, 8 kVpp is referred to as a starting point voltage of evaluation and analysis.

Considering the overall evolution of MA flow velocities, it presents a sharp jump at 12 kVpp from velocities below 0.5 m/s to in order of 2.0 m/s, after which it tends to increase reaching a maximum of 3.0 m/s. On the other hand, considering the evolution of MCZ and YSZ, it is straightforward to infer that MCZ has a significantly non-uniform and unstable behavior. For voltages between 8 and 10 kVpp, MCZ induces lower velocities than YSZ. Nevertheless, at 11 kVpp this dielectric material achieves its maximum, after which it drops sharply. Similarly, to alumina ceramic, YSZ starts to provide low velocities for low applied voltages, but after a particular value, in this case, 9 kVpp, this parameter rises considerably. The filamentary discharge verified on the YSZ surface was considered a strong limitation factor to further proceed with additional tests in the higher voltage range.

According to Fig. 4b, the following conclusions were driven for the 15 mm setup. MA alumina was once again the ceramic system that succeeded in inducing higher velocities, approximately 3.3 m/s, in comparison to the maximum achieved velocities, of about 0.9 m/s and 0.38 m/s, for MCZ, and YSZ, respectively. These results show the potential of the MA actuator for flow control applications which could induce velocity magnitudes close to 3.5 m/s, similar to the reported values in the literature for conventional Kapton actuators [23,26].

In parallel to the results of the setup with 10 mm, higher voltages were necessary to start recording any evidence of induced flow velocity for MA ceramic composite than for MCZ or YSZ. Similarly, to 10 mm results, MA is able to achieve higher flow velocities than the rest of the dielectrics tested. The MCZ and YSZ ceramics depict much more divergent behaviors and values than in the 10 mm setup. In this configuration, contrary to the previous one, MCZ tends to produce higher induced velocities than YSZ but still decreases after reaching its maximum of, approximately, 0.89 m/s. Once more, the filamentary discharge observed on the YSZ dielectric surface was found to be a solid limitation to further raise the applied voltage after 10 kVpp and reach a maximum induced velocity of 0.38 m/s.

Taking into consideration both configurations analyzed, i.e., 10 mm and 15 mm, some further general conclusions are emphasized (Table S3). MA manifested to be the sintered ceramic composite that was able to supply the plasma actuator device with higher induced flow velocities. Therefore, it is possible to claim that, in view of the active flow control focus, MA is the most efficient ceramic composite material. Furthermore, MA ceramic was more efficient in the 15 mm arrangement, whilst zirconia-based ceramics, MCZ, and YSZ performance, tended to improve in the 10 mm layout.

The heating of a DBD plasma actuator is considered one of the limiting factors of the operating performance during the plasma discharge process. More precisely, the variation of electrical power consumed by the device with the voltage increase trades off with the dielectric heating power oscillation during the discharge phenomenon, since a significant part of the power consumed is dissipated in the form of thermal energy [23,72,73].

Fig. 5 shows the thermographic images captured during the examination of the plasma discharge for each ceramic composite acting as a dielectric barrier for the DBD plasma actuator. Two aspects are remarked: (1) the delimited rectangle with a black line corresponds to the exposed electrode position and (2) the asymmetrical temperature distribution direction in the electrodes is predominant in the positive direction of the illustrated y-axis (referential in gray).

From Fig. 5, it was observed high discrepancies in terms of temperature magnitudes, i.e., maximum recorded temperatures, for each ceramic system were obtained. MA (Fig. 5a) showed the lowest achieved maximum temperature near the edge of the exposed electrode of approximately 46 °C, followed by MCZ (Fig. 5b) and YSZ (Fig. 5c) in the range of 60 °C and 150 °C, respectively. Additional information on the spatial variation of the temperature along the x- and y-axis can be found in Figs. S5 and S6.

The YSZ composite evidenced a considerably higher maximum temperature value of above 150 °C. The irregularities verified in the temperature fields are explained by several factors, such as the particular dielectric material's thermal properties. Additionally, it was noticed that the order of the maximum temperature achieved by the dielectric barriers, depicted in Fig. 5, coincides with the order of the power consumption indicated by Figs. 3a and 3b for an input voltage of 10 kVpp. The temperature asymmetries and irregularities shown along both sides of the exposed electrodes are attributed to the effects of the connections used in the mounted circuit, which tend to increase the temperature in their corresponding locations.

The temperature fields of the different ceramic dielectrics showed dissimilarities in function of the dielectric material. In detail, the YSZ

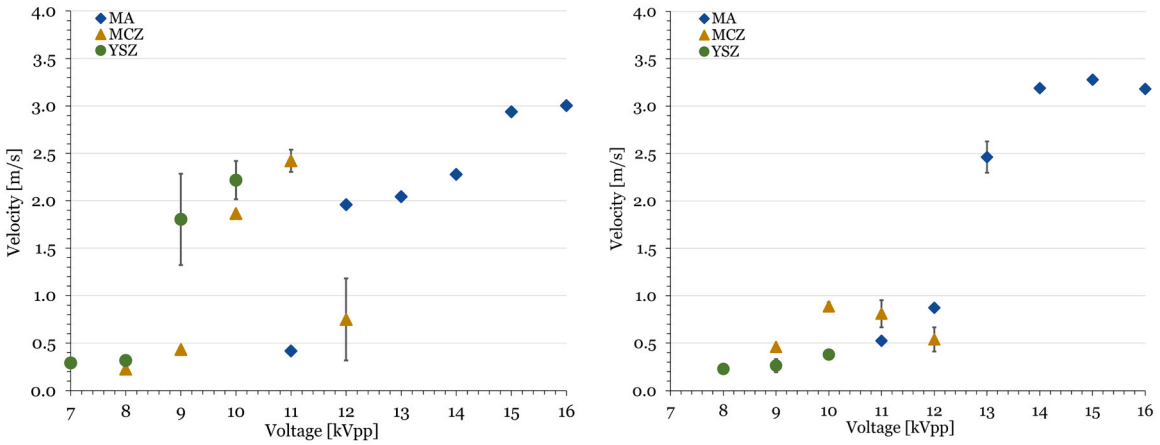

Fig. 4. Maximum induced flow velocities near the surface of the dielectric material for (a) 10 mm and (b) 15 mm setups at 24 kHz.

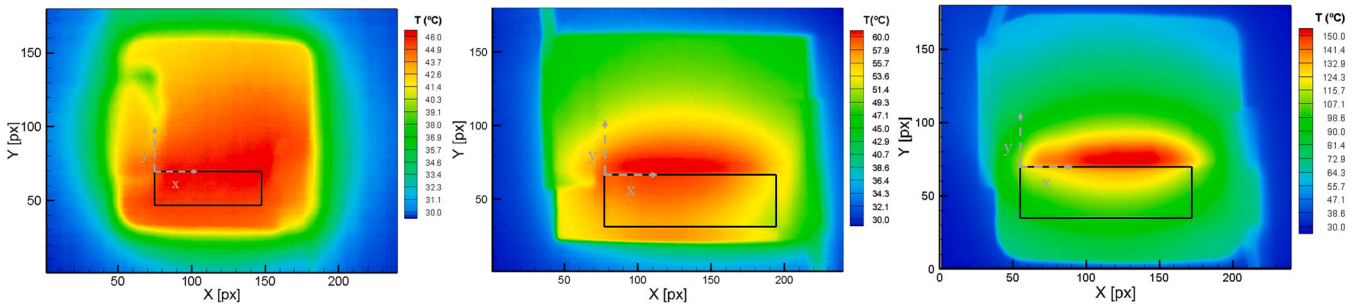

Fig. 5. Infra-red images for DBD plasma actuators with the different dielectric materials operating at 10 kVpp, and 24 kHz, (a) MA, (b) MCZ, and (c) YSZ.

temperature distribution field was much more concentrated than the rest of the materials. Contrastingly, MA depicted the most broadly distributed temperature levels across the dielectric surface. In addition, it is remarked that the highest temperatures in the YSZ material were mainly recorded at the edge of the exposed electrode (its frontal region), whilst for the remaining ceramic materials, it was obtained around the edge's area. The rate of spread of temperature across the ceramic samples described above is consistent with the thermal conductivity results discussed previously in Section 3.2. As Fig. 5 depicts, MA and MCZ ceramic systems are more prone to spread heat energy through the specimen than the YSZ composite.

As previously stated, part of the applied power is converted in the generation of flow velocities, whereas the remaining part is dissipated in the form of heat. Therefore, the dielectrics that registered a higher electrical power consumption tendentially are the ceramic composites which dissipate a higher amount of energy in the form of heat, that, in turn, increases the overall temperature of their surfaces. The results above agree with the discussion provided about power consumption (Fig. 3). An analysis of the maximum temperatures reached during the plasma discharge mechanism for each dielectric ceramic composite is presented in Fig. 6 for different input voltages. Whenever the error bar is not visible, it means that it is contained by the different ceramics' markers (green, yellow, and blue) due to the high precision of the equipment used – explained throughout 2.3.4. section. As expected, YSZ, which had a higher maximum temperature level achieved, (of above 150 °C, i.e., approximately, 155.4 °C at 10 kVpp) had also an abrupt rise in power consumed, followed by the MCZ (maximum temperature ceiling of 95.3 °C at 11 kVpp), and finally by the MA (maximum temperature ceiling of 78.7 °C at 14 kVpp). MA dielectric showed the slowest increase rate of power consumption with increasingly higher applied voltages.

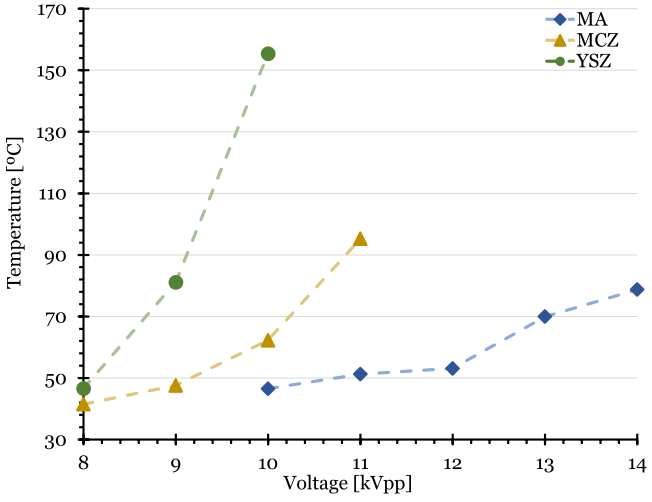

Fig. 6. Maximum temperature for DBD plasma actuators at different voltage levels and 24 kHz (average standard uncertainty of 2%).

The dashed lines on the graph serve as auxiliary temperature evolution data interpretation.

In general, the dielectric results of MA, for the active control flow, were superior to other composites. This behavior may be related to a phenomenon described typically in the volume DBDs as "electron avalanches": the rougher the dielectric material, the higher the number of "shallow traps". As a consequence of these "shallow traps", a higher content of accommodated electrons can be provided in the consecutive half-cycle discharges of the actuators. [74].

On the whole, the results obtained allow concluding that, although the MA-based actuator was demonstrated to be more efficient for active flow control purposes, the YSZ actuator presented a great potential to generate heat and increase the surface temperature, which makes it more suitable for simultaneous deicing and flow control applications [21]. Additionally, it is highlighted that the maximum temperature achieved by the YSZ actuator is quite larger than the temperatures usually reported in the literature for Kapton actuators (below 100 °C) [22]. In sum, the potential of ceramic composites as dielectric barriers for plasma actuators is demonstrated, not just for active flow control purposes but also for ice mitigation.

4. Conclusions

In this work, an experimental study was conducted regarding the feasibility of different ceramic composites – MA, MCZ, and YSZ – as dielectric barriers for DBD plasma actuators.

In terms of grain size, the YSZ microstructure was the one with the lowest size. The MA ceramic composite showed the highest porosity content (7%) and, therefore, lower densification, followed by YSZ (0.2%) and MCZ (0.05%). As a consequence, the MA ceramic had mechanical (Young's modulus, flexural strength, hardness, and fracture toughness) and thermal properties results (thermal conductivity and CTE) below the ones typically recognized in the dense bulk alumina ceramic. In contrast, MCZ and YSZ specimens were in line with the literature experimental results.

With respect to the DBD material-related characteristics, MA alumina-based ceramic had a higher operating limit (14 kVpp) and lower average electrical power consumption than both zirconia-based MCZ (12 kVpp) and YSZ (10 kVpp). Additionally, Lissajous figures, known as voltage-charge cyclograms, had consistent results in terms of power consumption considering the different ceramic dielectrics. With the electrical power consumption analysis, it was shown that all ceramic composites are capable of supporting a wide range of applied voltages without evidencing materials' functional degradation.

Furthermore, a trade-off between the distance of the Pitot tube to the edge of the exposed dielectric and the maximum velocity achieved, in the function of the applied voltage, was performed for induced flow velocity study purposes. Interestingly, MA ceramics were capable of achieving higher induced flow velocities than MCZ and YSZ for the two setups studied, i.e., 10 mm and 15 mm. Consequently, in view of the active flow control focus, MA ceramic is the most efficient material, once MA achieved velocities of, approximately, 3.0 m/s and 3.3 m/s for the

10 mm and 15 mm setups, respectively.

Finally, thermographic images showed that the ceramic system with higher power consumption was the one with a higher surface temperature. YSZ was the ceramic that heated the most (155.4 ºC), followed by MCZ (95.3 ºC), and MA (78.7 ºC) ceramics just as in the power consumption sequence. Thus, YSZ shows its suitability as a dielectric ceramic for DBD mechanisms for deicing applications due to its advantageous thermal properties.

Thus, this study shows that the suitable arrangement of morphological, mechanical, thermal, and functional properties of the developed ceramic composites allows them to be promising breakthrough materials for the development of DBD plasma actuators with improved performance and lifespan when compared with the current polymer-based solutions.

Declaration of Competing Interest

The authors declare that they have no known competing financial interests or personal relationships that could have appeared to influence the work reported in this paper.

Acknowledgments

This work was supported by the following projects and organisms: Portuguese Foundation for Science and Technology, I.P. (FCT, I.P.) FCT/MCTES through national funds (PIDDAC), under the R&D Unit C-MAST/Center for Mechanical and Aerospace Science and Technologies, reference: Project UIDB/00151/2020, and under the R&D Unit CF-UM-UP/Centro de Física das Universidades do Minho e do Porto, reference: Project UID/FIS/04650/2020. J.N.P. also thanks the FCT, I.P., European Social Fund (ESF), European Union (EU), and Regional Operational Program Centro 2020 and Norte 2020 for the grant SFRH/BPD/117838/2016. Funding from the Basque Government under the Elkartek program is also acknowledged.

Appendix A. Supporting information

Supplementary data associated with this article can be found in the online version at doi:10.1016/j.jeurceramsoc.2023.05.040.

References

[1] Tunmise Ayode Otitoju, Patrick Ugochukwu Okoye, Guanting Chen, Yang Li, Martin Onyeka Okoye, S. Li, Advanced ceramic components: Materials, fabrication, and applications, J. Ind. Eng. Chem. 85 (2020) 34–65, https://doi.org/10.1016/j.jiec.2020.02.002.

[2] J. Rödel, A.B.N. Kounga, M. Weissenberger-Eibl, D. Koch, A. Bierwisch, W. Rossner, M.J. Hoffmann, R. Danzer, G. Schneider, Development of a roadmap for advanced ceramics: 2010–2025, J. Eur. Ceram. Soc. 29 (9) (2009) 1549–1560, https://doi.org/10.1016/j.jeurceramsoc.2008.10.015.

[3] S.L. Swartz, Topics in electronic ceramics, IEEE Trans. Electr. Insul. 25 (5) (1990) 935–987, https://doi.org/10.1109/14.59868.

[4] E.C. Subbarao, Advanced ceramics—an overview, Sadhana 13 (1) (1988) 1–11, https://doi.org/10.1007/BF02811954.

[5] G. Petzow, R. Telle, R. Danzer, Microstructural defects and mechanical properties of high-performance ceramics, Mater. Charact. 26 (4) (1991) 289–302, https://doi.org/10.1016/1044-5803(91)90018-Y.

[6] W.O. Soboyejo, J.D. Obayemi, E. Annan, E.K. Ampaw, L. Daniels, N. Rahbar, Review of high temperature ceramics for aerospace applications, Adv. Mater. Res. 1132 (2016) 385–407, https://doi.org/10.4028/www.scientific.net/AMR.1132.385.

[7] K.O. Shvydyuk, J. Nunes-Pereira, F.F. Rodrigues, A.P. Silva, Review of ceramic composites in aeronautics and aerospace: a multifunctional approach for TPS, TBC and DBD applications, Ceramics 6 (1) (2023) 195–230, https://doi.org/10.3390/ceramics6010012.

[8] J. Li, C. Ma, S. Zhu, F. Yu, B. Dai, D. Yang, A review of recent advances of dielectric barrier discharge plasma in catalysis, Nanomaterials 9 (10) (2019) 1428, https://doi.org/10.3390/nano9101428.

[9] Y.P. Raizer, Production and Decay of Charged Particles, in: J.E. Allen (Ed.), Gas Discharge Physics, Springer-Verlag Berlin Heidelberg, Berlin, Germany, 1991, pp. 52–75.

[10] U. Kogelschatz, B. Eliasson, W. Egli, Dielectric-barrier discharges. principle and applications, C4-47-C4-66, J. Phys. IV Fr. 07 (C4) (1997) [, https://doi.org/10.1051/jp4:1997405.

[11] F.M.F. Rodrigues, Modelação experimental para otimização de atuadores a plasma com aplicações em termofluidodinâmica, Department of Electromechanical Engineering, University of Beira Interior, Covilhã, Portugal, 2019, p. 228.

[12] T. Abe, Y. Takizawa, S. Sato, N. Kimura, Experimental study for momentum transfer in a dielectric barrier discharge plasma actuator, AIAA J. 46 (9) (2008) 2248–2256, https://doi.org/10.2514/1.30985.

[13] N.D. Wilde, H. Xu, N. Gomez-Vega, S.R.H. Barrett, A model of surface dielectric barrier discharge power, Appl. Phys. Lett. 118 (15) (2021), 154102, https://doi.org/10.1063/5.0043339.

[14] J.R. Roth, Aerodynamic flow acceleration using paraelectric and peristaltic electrohydrodynamic effects of a One Atmosphere Uniform Glow Discharge Plasma, Phys. Plasmas 10 (5) (2003) 2117–2126, https://doi.org/10.1063/1.1564823.

[15] T. Corke, E. Jumper, M. Post, D. Orlov, T. McLaughlin, Application of weakly-ionized plasmas as wing flow-control devices, 40th AIAA Aerospace Sciences Meeting & Exhibit, ARC - Aerospace ResearchCentral, Reno, Nevada, USA, 14 January 2002 - 17 January 2002.

[16] T. Corke, B. Mertz, M. Patel, Plasma Flow Control Optimized Airfoil, 44th AIAA Aerospace Sciences Meeting and Exhibit, ARC - Aerospace Research Central, Reno, Nevada, USA, 09 January 2006 - 12 January 2006.

[17] N. Benard, E. Moreau, J. Griffin, L.N.Cattafesta Iii, Slope seeking for autonomous lift improvement by plasma surface discharge, Exp. Fluids 48 (5) (2010) 791–808, https://doi.org/10.1007/s00348-009-0767-6.

[18] E. Moreau, A. Debien, J.-M. Breux, N. Benard, Control of a turbulent flow separated at mid-chord along an airfoil with DBD plasma actuators, J. Electrost. 83 (2016) 78–87, https://doi.org/10.1016/j.elstat.2016.08.005.

[19] Y. Liu, C. Kolbakir, H. Hu, H. Hu, A comparison study on the thermal effects in DBD plasma actuation and electrical heating for aircraft icing mitigation, Int. J. Heat. Mass Transf. 124 (2018) 319–330, https://doi.org/10.1016/j.ijheatmasstransfer.2018.03.076.

[20] M. Abdollahzadeh, F. Rodrigues, J. Nunes-Pereira, J.C. Pascoa, L. Pires, Parametric optimization of surface dielectric barrier discharge actuators for ice sensing application, Sens. Actuators A: Phys. 335 (2022), 113391, https://doi.org/10.1016/j.sna.2022.113391.

[21] F. Rodrigues, M. Abdollahzadehsangroudi, J. Nunes-Pereira, J. Páscoa, Recent developments on dielectric barrier discharge (DBD) plasma actuators for icing mitigation, Actuators 12 (1) (2023) 5, https://doi.org/10.3390/act12010005.

[22] F.F. Rodrigues, J.C. Pascoa, M. Trancossi, Experimental analysis of dielectric barrier discharge plasma actuators thermal characteristics under external flow influence, J. Heat. Transf. 140 (10) (2018), https://doi.org/10.1115/1.4040152.

[23] J. Nunes-Pereira, F.F. Rodrigues, M. Abdollahzadehsangroudi, J.C. Páscoa, S. Lanceros-Mendez, Improved performance of polyimide Cirlex-based dielectric barrier discharge plasma actuators for flow control, Polym. Adv. Technol. 33 (4) (2022) 1278–1290, https://doi.org/10.1002/pat.5600.

[24] J. Pons, L. Oukacine, E. Moreau, J.M. Tatibouet, Observation of dielectric degradation after surface dielectric barrier discharge operation in air at atmospheric pressure, IEEE Trans. Plasma Sci. 36 (4) (2008) 1342–1343, https://doi.org/10.1109/TPS.2008.926856.

[25] M.T. Hehner, P. Warlitz, S. Pasch, T. Blank, J. Kriegseis, On the fabrication of durable dielectric-barrier discharge plasma actuators, 9th European Conference for Aeronautics and Space Sciences (EUCASS), EUCASS association, Lille, France, 27 June - 1 July, 2022.

[26] F.F. Rodrigues, J. Nunes-Pereira, M. Abdollahzadeh, J. Pascoa, S. Lanceros-Mendez, Comparative Evaluation of Dielectric Materials for Plasma Actuators Active Flow Control and Heat Transfer Applications, ASME 2021 Fluids Engineering Division Summer Meeting, ASME - The American Society of Mechanical Engineers, Virtual, Online, August 10–12, 2021.

[27] R. Pribyl, P. Stastny, M. Pazderka, J. Kelar, Z. Kelar Tucekova, M. Zemanek, M. Trunec, M. Cernak, Properties of $MgAl_2O_4$ doped alumina barrier layers for dielectric barrier discharge, J. Phys. D: Appl. Phys. 53 (50) (2020), 505202, https://doi.org/10.1088/1361-6463/abb0ba.

[28] S. Xiaozhen, Z. Yong, Q. Fuyang, W. Xiangrong, Effect of glass additions on $Ca_{0.8}Sr_{0.2}TiO_3$ ceramics as dielectrics for a cylindrical dielectric barrier discharge reactor in CO_2 plasma, Rare Met. Mater. Eng. 45 (12) (2016) 3037–3042, https://doi.org/10.1016/S1875-5372(17)30050-4.

[29] L. Ruixing, T. Qing, Y. Shu, Y. Yukishige, S. Tsugio, Decomposition oF Carbon Dioxide by the Dielectric Barrier Discharge (DBD) plasma using $Ca_{0.7}Sr_{0.3}TiO_3$ barrier, Chem. Lett. 33 (4) (2004) 412–413, https://doi.org/10.1246/cl.2004.412.

[30] D.-L. Bian, Y. Wu, M. Jia, C.-B. Long, S.-B. Jiao, Comparison between AlN and Al_2O_3 ceramics applied to barrier dielectric of plasma actuator*, Chin. Phys. B 26 (8) (2017), 084703, https://doi.org/10.1088/1674-1056/26/8/084703.

[31] ASTM, Standard Test Methods for Apparent Porosity, Water Absorption, Apparent Specific Gravity, and Bulk Density of Burned Refractory Brick and Shapes by Boiling Water, ASTM - American Society for Testing and Materials, 2022, p. 3.

[32] ASTM, Standard Test Method for Dynamic Young's Modulus, Shear Modulus, and Poisson's Ratio for Advanced Ceramics by Sonic Resonance, ASTM - American Society for Testing and Materials, 2020, p. 12.

[33] ASTM, Standard Test Method for Flexural Strength of Advanced Ceramics at Ambient Temperature, ASTM - American Society for Testing and Materials, 2019, p. 19.

[34] ASTM, Standard Test Method for Vickers Indentation Hardness of Advanced Ceramics, ASTM - American Society for Testing and Materials, 2019, p. 10.

[35] ASTM, Standard Test Method for Thermal Diffusivity by the Flash Method, ASTM - American Society for Testing and Materials, 2022, p. 11.
[36] ASTM, Standard Test Method for Linear Thermal Expansion of Solid Materials by Thermomechanical Analysis, ASTM - American Society for Testing and Materials, 2012, p. 5.
[37] M. Bryjak, I. Gancarz, K. Smolinska, Plasma nanostructuring of porous polymer membranes, Adv. Colloid Interface Sci. 161 (1) (2010) 2–9, https://doi.org/10.1016/j.cis.2010.09.004.
[38] D.F. Opaits, Dielectric Barrier Discharge Plasma Actuator for Flow Control, 2012.
[39] D. Ashpis, M. Laun, E. Griebeler, Progress toward Accurate Measurements of Power Consumption of DBD Plasma Actuators, 50th AIAA Aerospace Sciences Meeting including the New Horizons Forum and Aerospace Exposition, ARC - Aerospace Research Central, Nashville, Tennessee, USA, 09 January 2012 - 12 January 2012.
[40] J. Kriegseis, B. Möller, S. Grundmann, C. Tropea, Capacitance and power consumption quantification of dielectric barrier discharge (DBD) plasma actuators, J. Electrost. 69 (4) (2011) 302–312, https://doi.org/10.1016/j.elstat.2011.04.007.
[41] F.F. Rodrigues, J.C. Pascoa, M. Trancossi, Experimental Thermal Characterization of DBD Plasma Actuators, ASME 2017 International Mechanical Engineering Congress and Exposition, ASME - The American Society of Mechanical Engineers, Tampa, Florida, USA, November 3–9, 2017.
[42] G.B.J. de Boer, C. de Weerd, D. Thoenes, H.W.J. Goossens, Laser diffraction spectrometry: fraunhofer diffraction versus mie scattering, Part. Part. Syst. Charact. 4 (1–4) (1987) 14–19, https://doi.org/10.1002/ppsc.19870040104.
[43] K. Somton, K. Dateraksa, P. Laoratanakul, R. McCuiston, Shrinkage and properties of die pressed alumina produced from different granule sources, The Second Materials Research Society of Thailand International Conference, AIP Conference Proceedings, Pattaya, Thailand, July 10–12, 2019, p. 060003.
[44] P. Auerkari, Mechanical and physical properties of engineering alumina ceramics, Technical Research Centre of Finland Espoo1996.
[45] M. Asmani, C. Kermel, A. Leriche, M. Ourak, Influence of porosity on Young's modulus and Poisson's ratio in alumina ceramics, J. Eur. Ceram. Soc. 21 (8) (2001) 1081–1086, https://doi.org/10.1016/S0955-2219(00)00314-9.
[46] R.B. Heimann, Oxide Ceramics: Structure, Technology, and Applications, Classic and Advanced Ceramics: From Fundamentals to Applications, John Wiley & Sons,, Weinheim, Germany, 2010, pp. 175–252.
[47] Ceramic Material Comparison Chart. https://precision-ceramics.com/materials/comparison/. (Accessed Jan-2023.
[48] R.G. Munro, Evaluated material properties for a sintered alpha-alumina, J. Am. Ceram. Soc. 80 (8) (1997) 1919–1928, https://doi.org/10.1111/j.1151-2916.1997.tb03074.x.
[49] F. Ren, E.D. Case, A. Morrison, M. Tafesse, M.J. Baumann, Resonant ultrasound spectroscopy measurement of Young's modulus, shear modulus and Poisson's ratio as a function of porosity for alumina and hydroxyapatite, Philos. Mag. 89 (14) (2009) 1163–1182, https://doi.org/10.1080/14786430902915388.
[50] R.W. Rice, The porosity dependence of physical properties of materials: a summary review, Key Eng. Mater. 115 (1995) 1–20, https://doi.org/10.4028/www.scientific.net/KEM.115.1.
[51] A.P. Silva, F. Booth, L. Garrido, E. Aglietti, P. Pena, C. Baudín, Young's modulus and hardness of multiphase $CaZrO_3$-MgO ceramics by micro and nanoindentation, J. Eur. Ceram. Soc. 38 (4) (2018) 2194–2201, https://doi.org/10.1016/j.jeurceramsoc.2017.11.007.
[52] A.Rd.S. Cabral, Melhoria da resistência mecânica do compósito cerâmico CaZrO3-MgO com a adição de 3YSZ e 8YSZ, Department of Electromechanical Engineering, University of Beira Interior, Covilhã, Portugal, 2021, p. 44.
[53] J. Mamede, D.F. Macedo, A. Maceiras, A.P. Silva, Reinforcement of the ceramic matrix of CaO-ZrO_2-MgO with Al_2O_3 coarse particles, Ceramics 5 (1) (2022) 148–160, https://doi.org/10.3390/ceramics5010013.
[54] J. Nunes-Pereira, P.M.C. Carneiro, A. Maceiras, C. Baudín, A.P. Silva, Modelling of elastic modulus of $CaZrO_3$-MgO composites using isotropic elastic and anisotropic models, J. Eur. Ceram. Soc. 40 (15) (2020) 5882–5890, https://doi.org/10.1016/j.jeurceramsoc.2020.05.050.
[55] P.M.C. Carneiro, A. Maceiras, J. Nunes-Pereira, P.D. Silva, A.P. Silva, C. Baudín, Property characterization and numerical modelling of the thermal conductivity of $CaZrO_3$-MgO ceramic composites, J. Eur. Ceram. Soc. 41 (14) (2021) 7241–7252, https://doi.org/10.1016/j.jeurceramsoc.2021.06.044.
[56] M. Bauccio, M.L. Bauccio, ASM Engineering Materials Reference Book, Taylor & Francis1994.
[57] S.N. White, V.G. Miklus, E.A. McLaren, L.A. Lang, A.A. Caputo, Flexural strength of a layered zirconia and porcelain dental all-ceramic system, J. Prosthet. Dent. 94 (2) (2005) 125–131, https://doi.org/10.1016/j.prosdent.2005.05.007.
[58] Tosoh_Corporation, The fascinating world of Tosoh Zirconia. where value and potential are limited only by one's imagination. https://www.rbhltd.com/wp-content/uploads/2019/05/Tosoh-Zirconia-Brochure.pdf.
[59] F.A.B. Balça, Otimização de compósitos multifásicos de zircónia para aplicações termomecânicas aeronáuticas, Department of Electromechanical Engineering, University of Beira Interior, Covilhã, Portugal, 2022, p. 112.
[60] Jingjing Sun, Zijun Hu, Jiejie Zhou, Xiaoyan Wang, C. Sun, Thermal Properties of Highly Porous Fibrous Ceramics, in: E.C. International (Ed.) 5th International Conference on Porous Media and its Applications in Science and Engineering, Kona, Hawaii, USA, June 22–27, 2014.
[61] S.K. Rhee, Porosity-Thermal conductivity correlations for ceramic materials, Mater. Sci. Eng. 20 (1975) 89–93, https://doi.org/10.1016/0025-5416(75)90134-2.
[62] H. Zhao, F. Yu, T.D. Bennett, H.N.G. Wadley, Morphology and thermal conductivity of yttria-stabilized zirconia coatings, Acta Mater. 54 (19) (2006) 5195–5207, https://doi.org/10.1016/j.actamat.2006.06.028.
[63] S. Schafföner, C.G. Aneziris, H. Berek, J. Hubálková, A. Priese, Fused calcium zirconate for refractory applications, J. Eur. Ceram. Soc. 33 (15) (2013) 3411–3418, https://doi.org/10.1016/j.jeurceramsoc.2013.07.008.
[64] S. Schafföner, J. Fruhstorfer, C. Faßauer, L. Freitag, C. Jahn, C.G. Aneziris, Influence of in situ phase formation on properties of calcium zirconate refractories, J. Eur. Ceram. Soc. 37 (1) (2017) 305–313, https://doi.org/10.1016/j.jeurceramsoc.2016.08.017.
[65] F. Booth, L. Garrido, E. Aglietti, A. Silva, P. Pena, C. Baudín, $CaZrO_3$–MgO structural ceramics obtained by reaction sintering of dolomite-zirconia mixtures, J. Eur. Ceram. Soc. 36 (10) (2016) 2611–2626, https://doi.org/10.1016/j.jeurceramsoc.2016.03.027.
[66] X.Q. Cao, R. Vassen, D. Stoever, Ceramic materials for thermal barrier coatings, J. Eur. Ceram. Soc. 24 (1) (2004) 1–10, https://doi.org/10.1016/S0955-2219(03)00129-8.
[67] Compare by thermal expansion coefficient. https://nishimuraac.com/propertie/compare-by-thermal-expansion-coefficient/. (Accessed Jan-2023.
[68] J. Ferry, J. Rovey, Thrust Measurement of Dielectric Barrier Discharge Plasma Actuators and Power Requirements for Aerodynamic Control, 5th Flow Control Conference, ARC - Aerospace Research Central, Chicago, Illinois USA, 28 June 2010 - 01 July 2010.
[69] I. Biganzoli, R. Barni, A. Gurioli, R. Pertile, C. Riccardi, Experimental investigation of Lissajous figure shapes in planar and surface dielectric barrier discharges, J. Phys.: Conf. Ser. 550 (1) (2014), 012039, https://doi.org/10.1088/1742-6596/550/1/012039.
[70] M. Taheraslani, H. Gardeniers, Coupling of CH_4 to C_2 hydrocarbons in a packed bed DBD plasma reactor: the effect of dielectric constant and porosity of the packing, Energies 13 (2) (2020) 468, https://doi.org/10.3390/en13020468.
[71] S. Nimesh, Tools and Techniques for Physico-chemical Characterization of Nanoparticles Gene Therapy, Woodhead Publishing, 2013, pp. 43–63.
[72] F.J.J. Peeters, M.C.M. van de Sanden, The influence of partial surface discharging on the electrical characterization of DBDs, Plasma Sources Sci. Technol. 24 (1) (2015), 015016, https://doi.org/10.1088/0963-0252/24/1/015016.
[73] J. Pons, E. Moreau, G. Touchard, Asymmetric surface dielectric barrier discharge in air at atmospheric pressure: electrical properties and induced airflow characteristics, J. Phys. D: Appl. Phys. 38 (19) (2005) 3635, https://doi.org/10.1088/0022-3727/38/19/012.
[74] J. Ran, C. Li, D. Ma, H. Luo, X. Li, Homogeneous dielectric barrier discharges in atmospheric air and its influencing factor, Phys. Plasmas 25 (3) (2018), https://doi.org/10.1063/1.5019989.